Theoretical and experimental study of α-Sn deposited on CdTe(001)

J. A. Gómez,[1] Diana Guenzburger,[1] D. E. Ellis,[2] M. Y. Hu,[3] E. Alp,[3] E. M. Baggio-Saitovitch,[1] E. C. Passamani,[4] J. B. Ketterson,[2] and S. Cho[2]

[1]*Centro Brasileiro de Pesquisas Físicas, Rua Xavier Sigaud 150, 22290-180, Rio de Janeiro, R.J., Brazil*

[2]*Department of Physics & Astronomy and Materials Research Center, Northwestern University, Evanston, Illinois 60208*

[3]*Advanced Photon Source, Argonne, Illinois 60439*

[4]*Departamento de Física, Universidade Federal do Espírito Santo, 29060-900, Vitória-ES, Brazil*

(Received 16 September 2002; published 31 March 2003)

Gray tin films enriched by over 95% ^{119}Sn and grown by molecular beam epitaxy on CdTe(001) wafers are characterized by inelastic nuclear resonance spectroscopy and investigated theoretically by embedded-cluster density-functional theory methods. Experimental tin phonon densities of states are obtained via analysis of resonant scattering of the 23.88-keV nuclear transition, making use of a high-resolution spectrometer at the Advanced Photon Source. Conventional Mössbauer spectroscopy is used in the scattering mode to determine hyperfine parameters of the α-Sn phase and, after thermal treatment, the β phase. Electronic structure in the vicinity of Sn-Cd and Sn-Te interfaces is calculated in order to determine local charge transfer and changes in hyperfine parameters for ^{119}Sn atoms in the interface region. Although, due to sample thickness, both experiments reveal properties essentially of the bulk, the calculations allow investigation of surface and interface regions at an atomic level, thus providing complementary information. Effects of interlayer relaxation are explored.

DOI: 10.1103/PhysRevB.67.115340 PACS number(s): 73.90.+f, 73.20.−r

I. INTRODUCTION

The low-temperature diamond structure phase α-Sn (gray tin) has been the subject of much interest as a zero-gap semiconductor, which can be stabilized at room temperature when grown upon suitable crystalline substrates. The existence of in-plane lattice mismatch between substrate and overlayer, and the resulting strain in the tin overlayer provides a mechanism for opening the band gap which has intrigued many workers both from the theoretical point of view, and with an eye toward creating tunable band-gap photon detectors. The existence of quantum size effects on the band gap, due to film thickness, has also been demonstrated by resistivity measurements for a CdTe(001) film orientation[1] and by high-resolution electron energy loss spectroscopy for a CdTe(111) orientation.[2] The in-plane lattice mismatch of α-Sn with semiconducting CdTe(001) is only 0.18%, thus providing an attractive pair for multilayer $(\alpha\text{-Sn})_m(\mathrm{CdTe})_n$ superlattices, which have been studied theoretically by density functional (DF) band structure methods.[3] Ultrathin superlattices of composition $SnTe_2Cd$, $SnCd_2Te$, and Sn_2CdTe corresponding to (001) *monolayer* structures were also considered.[4] The well-known limitations of DF theory with respect to band gaps, particularly in the case of a sensitive material like α-Sn, restrict its predictive capabilities;[5] however, with some empirical adjustments, theoretical band structures can provide useful interpretations, including the pressure-dependent transition between α and β phases.[6] Svane *et al.* demonstrated the value of DF theory in calibration and interpretation of ^{119}Sn hyperfine interactions measured in a variety of tin compounds, including both monatomic phases.[7] The existence of one-dimensional quantum well states for (111) interfaces was also predicted on the basis of linear combination of atomic orbitals (LCAO) band structure calculations.[8]

The growth of α-Sn on differently oriented CdTe crystal faces has been demonstrated for polar (001),[9] (111),[10] and nonpolar (110)[11] interfaces and superlattices.[12] As polar surfaces typically reconstruct, and considerable perturbations could be expected at the semiconductor-Sn interface, it is interesting that monocrystalline α-Sn can be obtained under suitable deposition conditions for both Cd- and Te-terminated (111) substrates.[10] For high deposition temperatures it is not surprising that a reaction with the (111) substrate is observed, resulting in the formation of a certain amount of SnTe in the rock-salt phase and an intermixing zone extending over several bilayers.[10] The formation of a tetrahedrally coordinated $(Sn_{1-x}Cd_x)$ Te interface alloy layer has been proposed for Cd-terminated (111) interfaces, based upon core level and angle-resolved photoelectron spectroscopy (PES).[13] PES studies of (001) interfaces suggest an abrupt and nonreactive termination;[14] on the other hand, a layer-by-layer deposition and annealing study of the same interfaces by He scattering, low energy electron diffraction (LEED) and Auger electron spectroscopy (AES) gave a quite different picture.[15] The data of Ref. 15 were interpreted as vertical Sn diffusion leading to formation of ordered nanocrystalline SnTe at the interface, upon which α-Sn could grow. A study of CdTe(001)/α-Sn/CdTe single quantum well structures led to the conclusion that a Cd-stabilized surface is more suitable for clean interface growth.[16] It thus appears that fairly strong chemical interactions between Sn and the substrate atoms may determine the initial interface geometry, and that abrupt nonreactive interfaces may represent metastable structures. In this context, a pseudopotential DF study of lattice stability in $Cd_xSn_{1-x}Te$ solid solutions is quite interesting, showing a pronounced preference for the rock-salt structure over most of the mixing range.[17]

In this paper we present experimental and theoretical studies of α-Sn films deposited on CdTe(001) surfaces, using ^{119}Sn inelastic nuclear resonant scattering (INRS), Möss-

bauer spectroscopy (MS), and DF embedded cluster methods. The INRS data permit the extraction of tin-site vibrational structure and its comparison with bulk tin experiment and theory, while the MS data reveal details of the electronic structure around the tin site. DF calculations are used to elucidate the variation of electronic properties across the Sn/CdTe interface region, in comparison with bulk and free surface structures. The remainder of the paper is organized as follows: Sample preparation and experimental data are given in Sec. II, the theoretical methodology is outlined in Sec. III, and an analysis of theoretical results is given in Sec. IV. Our conclusions are presented in Sec. V.

II. EXPERIMENT

A. Sample preparation

Films of α-Sn were grown by molecular beam epitaxy on semiconducting CdTe(001) substrates of 1 mm thickness. Prior to tin deposition a 3000 Å CdTe buffer layer was grown on the substrate at a temperature of 250 °C. During tin deposition a growth rate of 0.4 Å per second was maintained, at temperature 0 °C. Samples of thickness 2000 Å were prepared with an enrichment of over 95% in ^{119}Sn and verified to have a (1×1) reconstructed surface by *in situ* reflection high-energy electron diffraction (RHEED). The in-plane lattice mismatch of α-Sn with the CdTe substrate was found to be only 0.18%, consistent with the bulk lattice constant of 6.49 Å.

B. Inelastic nuclear resonant scattering

The phenomenon of inelastic nuclear resonant scattering with synchrotron radiation permits the use of nuclear resonant isotopes as probes to study local vibrational dynamics of the isotopes in diverse solid state and molecular structures.[18–21] Within the context of harmonic lattice approximation, it is possible to map out the localized vibrational density of states (DOS), going beyond the capabilities of traditional Mössbauer spectroscopy. The nuclear resonant energy for ^{119}Sn is 23.88 keV; two monochromators were designed and constructed at the Advanced Photon Source with energy resolutions of 3.6 and 1.0 meV in the 24 keV X-ray energy range, each using two flat perfect silicon crystals.[22,23] The typical photon flux within this energy bandwidth is about 3×10^8 photons per second at a 100 mA storage ring current. Enriched powder samples of SnO, SnO_2, and $CaSnO_3$ were studied to characterize the vibrational DOS of oxides and its response to pressure. Enriched and natural foils of metallic β-Sn (white tin, double body-centered tetragonal, stable above 13.2 °C) were also studied at room temperature, under normal pressure and at high pressures, where a transition to simple body-centered tetragonal structure occurs. The very small *f* factor (recoilless fraction) of 0.03 and overwhelming multi-phonon terms prevented extraction of a quantitative DOS for β-Sn samples at room temperature. Fortunately, the stabilized α-Sn films have an *f* factor of 0.16, sufficiently large to permit separation of single-, double-, and higher-order phonon excitations of the measured phonon spectrum.

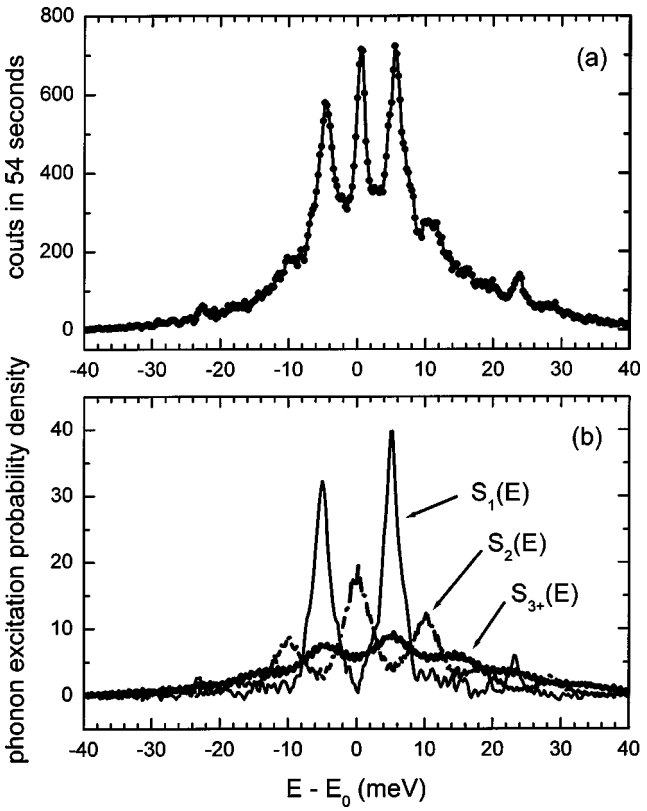

FIG. 1. (a) INRS spectrum for α-Sn/CdTe(001). Panel (b) shows separated one- and two-phonon probability densities $S_1(E)$ and $S_2(E)$, and three-phonon and higher probability densities $S_{3+}(E)$. $E-E_0$ is the X-ray energy minus the nuclear transition energy.

In order to increase the count rate, we put two α-Sn films side by side along the X-ray beam direction and made the X-ray beam incident at a shallow angle. The electronic absorption length is 133 μm in α-Sn for 23.88 keV X-rays, and the elastic nuclear resonant absorption length is only 0.24 μm. The inelastic nuclear resonant absorption is much weaker and has longer absorption length. Since the films are 0.2 μm thick, the entire sample contributes to the INRS signal, and since the surface and Sn/CdTe interface contribute very little to the total, we essentially measure the bulk property of α-Sn.

The INRS spectrum is shown, along with resulting one-, two-, and three-and higher-phonon excitation probability densities in Fig. 1. The energy range scanned in the actual experiments was 160 meV, centered at 23.88 keV, the nuclear resonant energy of ^{119}Sn. In the figure, the data are presented in a smaller energy range for greater legibility. The recoiless fraction factor *f* and derived lattice dynamics properties[24,25] (in the context of a harmonic lattice approximation) are listed in Table I. A comparison of the INRS one-phonon DOS with results of a density functional pseudopotential band structure calculation on bulk α-Sn[26] is given in Fig. 2. Coherent inelastic neutron scattering experiments have also been done,[27] resulting in dispersion curves along a few high symmetry directions, which compare well with the above-cited electronic structure theory and lattice dynamics modeling. By comparing these experimental data and theory, we can say

TABLE I. Recoilless transition factor f, mean kinetic energy per atom $\langle T\rangle$, mean force constant $\langle K\rangle$, and estimated mean displacement $\langle u\rangle$ of α-Sn derived from INRS measurements. From Refs. 18, 19.

f	$\langle T\rangle$ (meV)	$\langle K\rangle$ (N/m)	$\langle u\rangle$ (Å)
0.16(2)	13.4(2)	155(16)	0.19

that these gray tin films exhibit characteristic bulk properties, with no sign of severe stress- or interface-related anomalies. It would be very interesting to carry out similar measurements on multilayer Sn/CdTe structures with individual layer thickness of less than 10 Å in order to enhance and examine interface effects. A recent study of Sn/amorphous-Si multilayers[28] showed that in a 10 Å-thick layer, Sn maintains an α-Sn-like structure but is influenced by adjacent amorphous-Si layers and also becomes amorphous. Unfortunately, for Sn/CdTe the attempts to grow multilayers have had limited success, as apparently interface roughness and disorder grows with the number of deposited layers.[10]

C. Conversion electron Mössbauer spectroscopy (CEMS)

The Mössbauer measurements were carried out at Centro Brasileiro de Pesquisas Físicas at room temperature in a conventional CEMS chamber with a gas mixture of 96% of He and 4 % of CH_4, for as-received and annealed thin films. The CEMS spectra were obtained using a 12 mCi metastable ^{119m}Sn source in a $BaSnO_3$ matrix, in constant acceleration

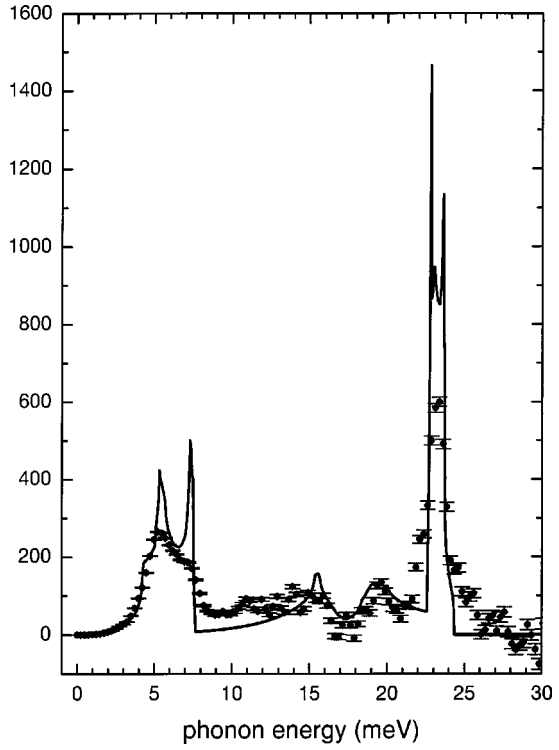

FIG. 2. Partial phonon density of states for α-Sn from INRS measurements, together with *ab initio* results of Ref. 26.

TABLE II. Mössbauer parameters for bulk tin phases, α-Sn(001) surface layer and Sn/CdTe(001) films at room temperature and after annealing at ~130 °C.

	Isomer shift (mm/sec)	η	Quadrupole splitting (mm/sec)
α-Sn phase expt.	−0.52(2.02)[a]	–	0
theory	−0.66[b]	–	
	−0.41[−0.51][c]		
α-Sn(001) surface layer (theory)	+0.67[c]	0.42[d]	−2.85[d]
β-Sn phase expt.	0.00(2.54)[a]	0	|0.43|[f]
theory	0.00[b]	0	|0.36|[b]
	0.00[c]	0	−0.75[d]
Sn/CdTe(001) (as-received)expt.[e]	−0.58(1.96)	0	0
Sn/CdTe(001)	−0.58(1.96)	α-phase:26%	0
(130 °C) expt.[e]	0.00 (2.54)	β-phase:23%	|0.65|
	0.41(2.95)	alloy:48%	0
	−2.54 (0.00)	oxide:3%	0

[a]Reference 29, with respect to β-Sn. Values in parentheses are relative to the common SnO_2 reference.

[b]Reference 7. Calibration factor $\alpha=0.092$ and nuclear moment $|Q|=12.8$ fm^2 fitted to the data.

[c]This work, with respect to β-Sn reference; calibration factor $\alpha=0.0844$ fitted to Sn^{+2} and Sn^{+4} data (Ref. 37). The value in square brackets is for calibration factor $\alpha=0.092$ of Ref. 7. Further details appear in Table V.

[d]This work. The value of the nuclear moment $Q=-0.109b$ is from Ref. 39; further details appear in Table VI.

[e]This work. Cd or Te ordering at interface undetermined. Relative spectral areas of each component are given in the third column.

[f]From Ref. 30.

mode. For all experiments, source and absorber were kept at the same temperature during the measurements. The CEMS spectra were fitted using a single line for the as-received sample, and a set of single lines and quadrupolar components for the annealed Sn/CdTe samples. Heat treatments up to temperatures of 150 °C were done in as-received samples inside a high temperature Mössbauer furnace, with a vacuum condition better than 10^{-5} mbar.

The CEMS spectrum of the as-received samples, not shown, displays a single line with an IS value of about 1.96 mm/s and therefore associated with the α-Sn phase, confirming the INRS results, and consistent with values previously published for bulk α-Sn,[29,7] as shown in Table II. On the other hand, CEMS spectra of the annealed samples show basically that (i) an enhancement of an oxidized (SnO_2) fraction of the film as temperature and time of annealing increase; and (ii) an irreversible change in crystalline structure of the film as the annealing temperature increases, i.e., changes from α-Sn to β-Sn and to a new Sn phase, with IS close to 2.95 mm/s.

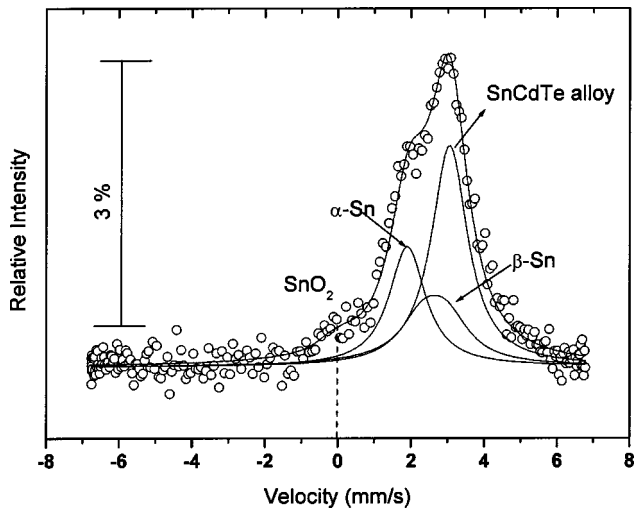

FIG. 3. Conversion electron Mössbauer spectra of Sn/CdTe(001), after heat treatment at 130 °C.

The structural transition is clearly seen in Fig. 3, which shows the CEMS spectrum of the film annealed at 130 °C. This spectrum was fitted with four components: a subspectrum with hyperfine parameters of SnO_2 (3% of the spectrum area); a single line with an IS of α-Sn (26% of the spectrum area); a doublet with an IS of 2.54 mm/s and quadrupole splitting (QS) of 0.65 mm/s (23% of spectrum area) which we identify with bulk β-Sn (white tin) values[7,29,30] and finally a broad single line with an IS of 2.95 mm/s. The broadening effect observed for this new line with an IS of 2.95 mm/s may be an indication for an existence of a small quadrupolar interaction around Sn atoms. This component may be attributed to alloy formation at the interface between the Sn and the substrate. However, it is difficult to understand why such a large fraction of this component is observed at such low annealing temperatures, unless the interface is somewhat unstable.

III. THEORETICAL METHODOLOGY

A. Embedded cluster density functional method

Density-functional calculations have been performed using the discrete variational (DV) method in the local density approximation[31] (LDA) for studying the structural and hyperfine properties of α-Sn/CdTe(001) heterojunctions. The DV method is widely described in the literature;[32] here, we will give only a brief description of its main features. In this method, the solid is represented by a finite cluster of atoms, embedded in the potential of a set of atoms representing the external crystal environment. The one-electron orbitals are obtained by solving the Kohn-Sham equations in a three-dimensional grid where the potential field is a functional of the electronic charge density $\rho(\mathbf{r})$. These one-electron orbitals are constructed as linear combinations of numerical atomic orbitals, (LCAO), which in turn are obtained by density-functional calculations in the LDA for free ions or atoms. The basis set configurations are typically optimized by reference to the self-consistent charge distribution. For the exchange and correlation potential terms in the effective Hamiltonian, we employed the parametrization of Vosko, Wilk, and Nusair of the Ceperley-Alder results.[33] For total energy calculations, we employed the gradient corrections to the LDA developed by Becke[34] and Perdew[35] for the exchange and correlation terms, respectively. To prevent a spurious migration of electronic charge of cluster atoms to external atoms, for the latter a simple pseudopotential is used, consisting of a truncation of the attractive potential in the core region to simulate effects of the Pauli exclusion principle. We made extensions to the existing DV codes so as to describe two-dimensionally periodic bicrystalline and multilayer interfaces involving both metallic and ionic structures. In order to deal efficiently with charge transfer and long-range interactions in these ionic systems, an Ewald-summation method for surfaces developed by Parry[36] was adapted for the construction of the multilayer bicrystal Coulomb potential.

A model density is employed to facilitate the calculation of the Coulomb interaction term in the matrix elements of the Kohn-Sham Hamiltonian. The model density is given as a multipolar expansion centered at the atomic nuclei, using radial functions constructed from the LCAO set and additional highly localized analytic functions. This model density is fitted by least-squares error minimization to the exact charge density. In the present calculations, terms of $l=0$ only have been considered. The criterion of convergence considered in self-consistent calculations was a difference of $<10^{-5}$ in the electronic charge density-model between two successive cycles.

The $4d$, $5s$, and $5p$ basis atomic orbitals (valence orbitals) were considered in the variational approach for the Cd, Te, and Sn atoms of the cluster; the inner atomic core orbitals were considered frozen. The valence orbitals were explicitly orthogonalized against core orbitals in the first iteration. Atomic orbital occupancies were analyzed, using a Mulliken-type population analysis, based on the LCAO expansion coefficients. The orbital occupations in turn served to define partial densities of states (PDOS) useful in a energy-band type of description of state distributions. The self-consistent wavefunctions were further used to generate graphical displays of interface charge density, and to calculate hyperfine properties relevant to Mössbauer measurements on ^{119}Sn.

The transition used for ^{119}Sn Mössbauer spectroscopy is the 23.875 keV γ-ray from the first excited state with $I=\frac{3}{2}$ to the ground state with $I=\frac{1}{2}$. For the calculation of the IS, we employed the expression:

$$\mathrm{IS}=\alpha S'(Z)[\rho_a(0)-\rho_b(0)] \tag{1}$$

where the calibration constant $\alpha=0.0844a_o^3$ mm/s was obtained by correlating the experimental IS of a series of Sn(II) and Sn(IV) compounds with their respective electronic charge densities at the Sn nucleus obtained by DF calculations with the DV method.[37] Here $S'(Z)$ is the correction factor for relativistic effects, which for ^{119}Sn is 2.306,[38] and $[\rho_a(0)-\rho_b(0)]$ is the difference between the non-relativistic electronic charge density at the tin nucleus of system a and reference system b. Recently, the value of α was also calcu-

lated by comparing experimental IS of tin compounds with relativistic electronic charge densities calculated with the Full-Potential Linear-Muffin-Tin-Orbital (FP-LMTO) method within the LDA.[7] Their value of $\alpha = 0.092 a_o^3$ mm/s is similar to the one obtained in Ref. 37.

The $I = \frac{3}{2}$ to $I = \frac{1}{2}$ transitions result in two γ rays due to the quadrupole moment Q of the excited state, with an energy difference (QS) given by the expression

$$\mathrm{QS} = \frac{1}{2} e Q V_{ZZ} \left(1 + \frac{\eta^2}{3} \right)^{1/2}, \tag{2}$$

where V_{ZZ} is the main component of the electric field gradient and η is the asymmetry parameter, defined as $\eta = (V_{XX} - V_{YY})/V_{ZZ}$ with the convention $|V_{ZZ}| > |V_{YY}| \geqslant |V_{XX}|$. The components of the traceless electric-field gradient tensor V_{ij} at the Sn nucleus are calculated by the expression (in atomic units)

$$V_{ij} = -\int \rho(\mathbf{r})(3x_i x_j - \delta_{ij} r^2)/r^5 d\mathbf{r} + \sum_q Z_q^{\mathrm{eff}} (3x_{qi} x_{qj} - \delta_{ij} r_q^2)/r_q^5, \tag{3}$$

where the first and second terms are the electronic and point-ion contributions respectively. $\rho(\mathbf{r})$ is the valence electron charge density and Z_q^{eff} is the effective nuclear point charge (nuclear charge screened by core electrons) of atoms surrounding the Sn probe. The value of Q employed here was $-0.109b$ obtained experimentally by comparing Mössbauer spectroscopy and perturbed angular correlation measurements on tin impurities in a Cd host.[39] The magnitude $|Q| = 0.128b$ was also estimated in Ref. 7 by comparing experimental QS values of tin compounds with their respective calculated electric-field gradients.

B. Interface and cluster geometry

In order to study the properties of α-Sn/CdTe(001) heterojunctions, we considered two types of structural configuration at the interface layers.

(1) Sn layers with diamond crystalline structure on a CdTe(001) surface terminating in a Cd layer. Such clusters will be henceforth called α-Sn/CdTe.

(2) Sn layers with diamond structure on a CdTe(001) surface terminating in a Te layer. Such clusters will be called α-Sn/TeCd.

The variational clusters were embedded in a potential field generated by more than 30 000 external atoms, generating the semi-infinite diamond α-Sn and zinc-blende CdTe host structures. For both half-crystals the experimental lattice parameter of CdTe (6.48 Å) was employed. The electronic configurations of the embedding atoms were obtained by self-consistent cluster calculations on the constituent bulk materials, projected onto Mulliken populations. The charge transfer from Cd to Te was found to be approximately $1.25e$ in the bulk compound, with effective configurations for the valence orbital basis of: $4d^{10}5s^{0.49}5p^{0.26}$ for Cd, $4d^{10}5s^{1.95}5p^{5.30}$ for Te and $4d^{10}5s^{1.66}5p^{2.34}$ for α-Sn. A total of 79 atoms was considered for the construction of the clusters mentioned above and distributed as follows: for the α-Sn segment, we considered 46 atoms distributed in five layers; for the CdTe segment we considered 33 atoms distributed in four layers (two Cd layers and two Te layers). Table III shows a typical distribution of the Cd, Te, and Sn atoms at each layer for the clusters considered; here I indicates the interface layer, $I-1$ the first neighbor layer to I, and so on. Local properties are calculated at the most central atom of each layer, to avoid spurious effects of the surface of the clusters.

TABLE III. Distribution of Cd, Te, and Sn atoms in α-Sn/CdTe and α-Sn/TeCd clusters.

α-Sn/CdTe		α-Sn/TeCd	
layer	N^0 atoms	layer	N^0 atoms
Sn_{I-4}	5	Sn_{I-4}	5
Sn_{I-3}	8	Sn_{I-3}	8
Sn_{I-2}	12	Sn_{I-2}	12
Sn_{I-1}	8	Sn_{I-1}	8
Sn_I	13	Sn_I	13
Cd_I	8	Te_I	8
Te_{I-1}	12	Cd_{I-1}	12
Cd_{I-2}	8	Te_{I-2}	8
Te_{I-3}	5	Cd_{I-3}	5

For the purpose of comparison with the interfaces described above, electronic structure calculations of α-Sn and CdTe pure crystals have been performed with diamond and zinc-blende crystalline structures respectively using the experimental lattice parameter of CdTe. In this way cluster 'surface states' and any other effects due to finite cluster size can be identified and compensated for. 79- and 85-atom clusters were considered to represent the α-Sn and CdTe pure crystals, respectively. For the construction of the cluster representing α-Sn, we considered nine layers. For the construction of CdTe clusters, we considered two different structural configurations.

(i) A cluster composed of five Cd layers and four Te layers, with a central Cd layer. This cluster is called CdTe(I), and is appropriate for comparison with α-Sn/TeCd clusters.

(ii) A cluster composed of five Te layers and four Cd layers, with a central Te layer. This cluster is called CdTe(II), and is appropriate for comparison with α-Sn/CdTe clusters.

For the sake of further comparisons with electronic structure of tin in different environments, we carried out analogous calculations on a free (001) surface of α-Sn and on bulk β-Sn, using clusters of 46 and 79 atoms, respectively.

IV. THEORETICAL RESULTS

To explore the equilibrium structural configuration at the interface layers in the heterojunctions, we calculated the total energy of the embedded clusters, changing only the distance between the two half-infinite crystals. All other structural parameters were kept constant; i.e., differential perpendicular relaxation and transverse reconstructions were not consid-

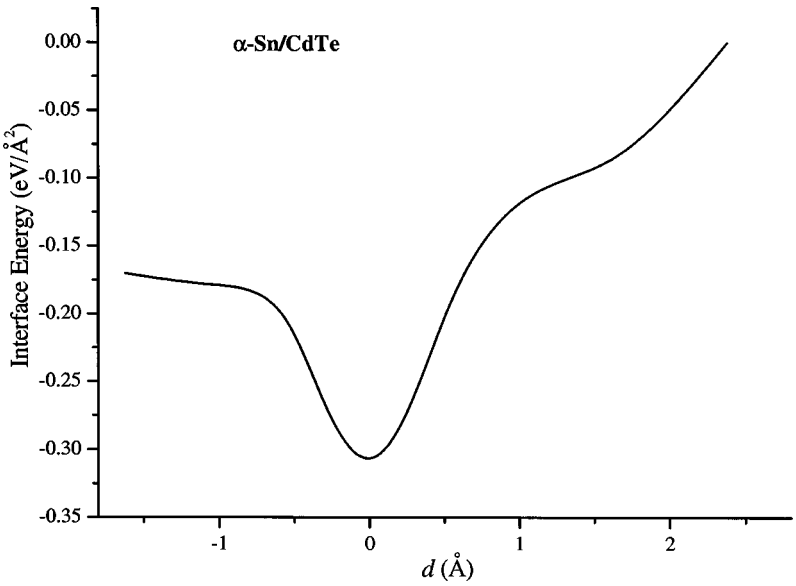

FIG. 4. Interfacial energy of α-Sn/CdTe. d is the distance between the interface layers (Cd_I-Sn_I).

ered. The relative interfacial energies (total energy minus energy of isolated atoms in the basis configuration, divided by interface area) vs distance between the interface layers are shown in Figs. 4 and 5 for α-Sn/CdTe and α-Sn/TeCd clusters respectively. Negative distances in Fig. 4 indicate overlapping between the CdTe and α-Sn crystals. In the ideal unrelaxed interface the interplanar spacing is 1.62 Å, and we see that the energy minimum for the Sn/TeCd interface is slightly expanded with respect to this value. On the contrary, the energy minimum for the Sn/CdTe interface occurs exactly where tin and cadmium lie in the same layer, essentially forming a monolayer intermetallic SnCd compound. Evidence of such an interface alloy layer was found via valence band photoemission studies of (111) heterostructures.[13] Similar self-consistent-field and total energy calculations were carried out for smaller 53-atom clusters, giving essentially identical energy minima; thus we consider that the predicted structure is reliable, within the limitations of a single interplanar-distance variable. The energy-minimum geometries of Sn/CdTe and Sn/TeCd interfaces are shown in Figs. 6 and 7, respectively.

Electronic properties can be rapidly surveyed by examining self-consistent Mulliken populations and the associated partial DOS (PDOS). In Table IV we present a layer-by-layer comparison of populations and charges, which demonstrate the variable charge transfer and atomic configurations across the selvage region. Selected PDOSs are presented in Figs. 8 and 9, representing the $5sp$ valence band distribution of selected sites in the vicinity of the Fermi level. The Cd $4d$ levels are also included in the energy interval shown; the Te $4d$ is located at considerably lower energies. The variability of the Sn PDOS with bulk state, surface, and interface environments is evident in Fig. 8, while the perturbation of Cd and Te distributions are shown in Fig. 9. Although the cluster method, with its discrete level structure, can not reliably predict the existence or size of band gaps, we immediately no-

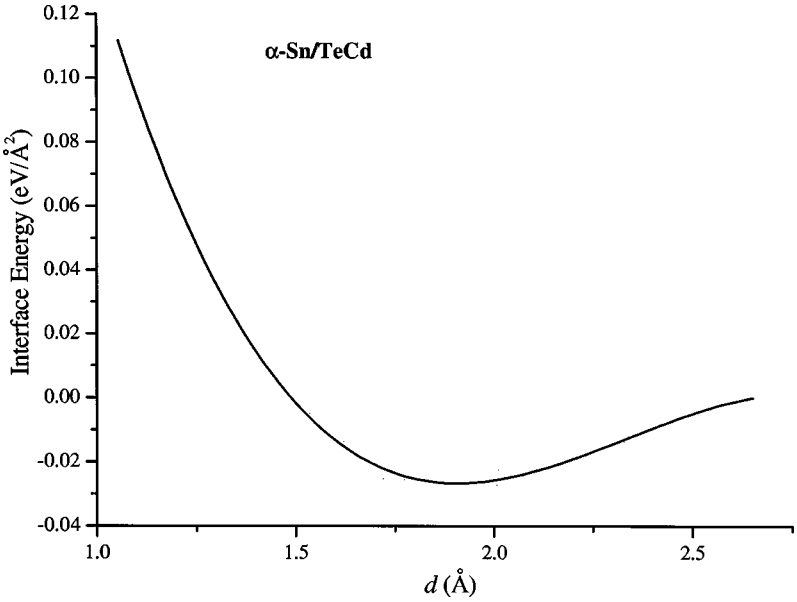

FIG. 5. Interfacial energy of α-Sn/TeCd. d is the distance between the interface layers (Te_I-Sn_I).

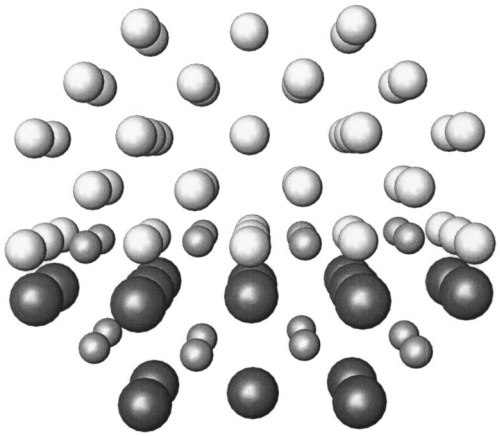

FIG. 6. 79-atom cluster representing the α-Sn/CdTe heterojunction in the equilibrium structural configuration. The white, gray, and black spheres represent Sn, Cd, and Te atoms respectively.

tice [Fig. 8(a)] the very low Sn DOS for $E \sim E_F$ in α-Sn, compared to all other cases, including the free surface [Fig. 8(b)]. The tin PDOS at the Sn/Te and Sn/Cd heterojunctions [Figs. 8(c) and 8(d)] shows a notable band broadening due to mixing between the two species. For Sn/Te we see some evidence of bonding structure at the bottom of the valence band (VB), nonbonding states $\sim E_F$, and antibonding states in the unoccupied region as would be expected for ionic-covalent bonding. The Sn_ICd_I interlaced minimum-energy layer has a typical metallic appearance, consistent with electronic density maps presented below. The summed Cd and Te PDOSs shown in Fig. 9 for bulk [(a) and (b)] and Sn/Te (c), and Sn/Cd (d) interface configurations, each representing two atomic layers, show a VB with a strong peak dominated by Cd 4*d* and an extremely low intensity around E_F which can be associated with the band gap (1.44 eV at 300 K) of the host CdTe semiconducting compound. The excellent agreement between CdTe(I) and CdTe(II) bulk cluster configurations confirms the overall accuracy of the cluster representation and its independence of coordinate origin. A shift

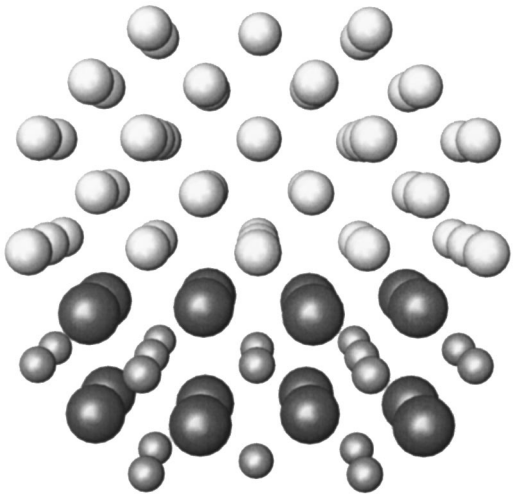

FIG. 7. 79-atom cluster representing the α-Sn/TeCd heterojunction in the equilibrium structural configuration. Sphere specifications as in Fig. 6.

TABLE IV. Mulliken population of valence orbitals and charges Q at the central atoms in I and I-1 layers for α-Sn/CdTe and α-Sn/TeCd clusters, at the central atoms in S (surface) and S-1 layers for α-Sn surface and at the central atoms Sn_c for α-Sn and β-Sn bulk. The interface layers distance d is given in Å.

Cluster	Interface d	site	Population $4d$	$5s$	$5p$	Q
α-Sn/CdTe	1.62	Sn_{I-1}	9.99	1.68	2.44	−0.10
		Sn_I	9.99	1.77	2.18	0.06
		Cd_I	9.93	0.66	0.28	1.13
		Te_{I-1}	10.00	1.96	5.00	−0.96
	0.53	Sn_{I-1}	9.99	1.70	2.36	−0.04
		Sn_I	9.99	1.67	2.30	0.04
		Cd_I	9.88	0.61	0.37	1.14
		Te_{I-1}	10.00	1.95	4.90	−0.85
	0.00[a]	Sn_{I-1}	9.99	1.69	2.31	0.01
		Sn_I	9.99	1.68	2.35	−0.02
		Cd_I	9.88	0.62	0.37	1.12
		Te_{I-1}	10.00	1.93	4.85	−0.78
	−0.79	Sn_{I-1}	9.99	1.67	2.17	0.17
		Sn_I	9.99	1.74	2.42	−0.14
		Cd_I	9.89	0.70	0.44	0.96
		Te_{I-1}	10.00	1.87	4.72	−0.59
α-Sn/TeCd	1.85[a]	Sn_{I-1}	9.99	1.67	2.36	−0.02
		Sn_I	9.99	1.78	2.15	0.08
		Te_I	10.00	1.93	5.23	−1.15
		Cd_{I-1}	9.96	0.67	0.36	1.01
	1.62	Sn_{I-1}	9.99	1.66	2.32	0.03
		Sn_I	9.99	1.75	2.24	0.01
		Te_I	10.00	1.91	5.19	−1.10
		Cd_{I-1}	9.96	0.69	0.36	0.99
	1.53	Sn_{I-1}	9.99	1.66	2.30	0.05
		Sn_I	9.99	1.74	2.28	−0.01
		Te_I	10.00	1.90	5.19	−1.08
		Cd_{I-1}	9.96	0.69	0.37	0.98
	1.06	Sn_{I-1}	9.99	1.64	2.26	0.11
		Sn_I	9.99	1.67	2.56	−0.21
		Te_I	10.00	1.86	5.12	−0.97
		Cd_{I-1}	9.96	0.71	0.38	0.95
α-Sn surface	-	Sn_S	9.99	1.85	2.01	0.15
	-	Sn_{S-1}	9.99	1.65	2.48	−0.12
α-Sn bulk	-	Sn_c	9.99	1.64	2.37	0.00
β-Sn bulk		Sn_c	9.99	1.73	2.28	0.00

[a]Minimum-energy configuration.

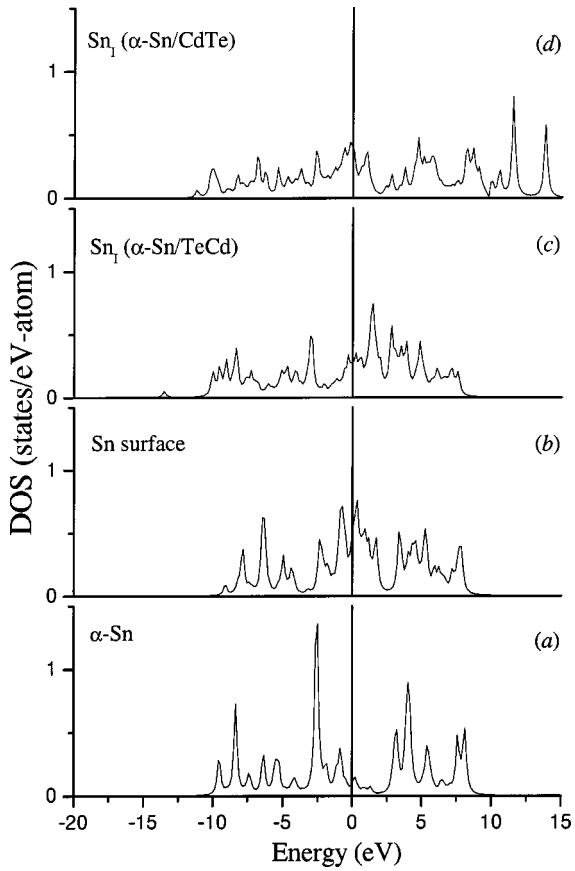

FIG. 8. Tin partial densities of states in different environments: (a) bulk α-Sn, (b) free (001) α-Sn surface layer, (c) α-Sn/TeCd interface layer, and (d) α-Sn/CdTe interface layer.

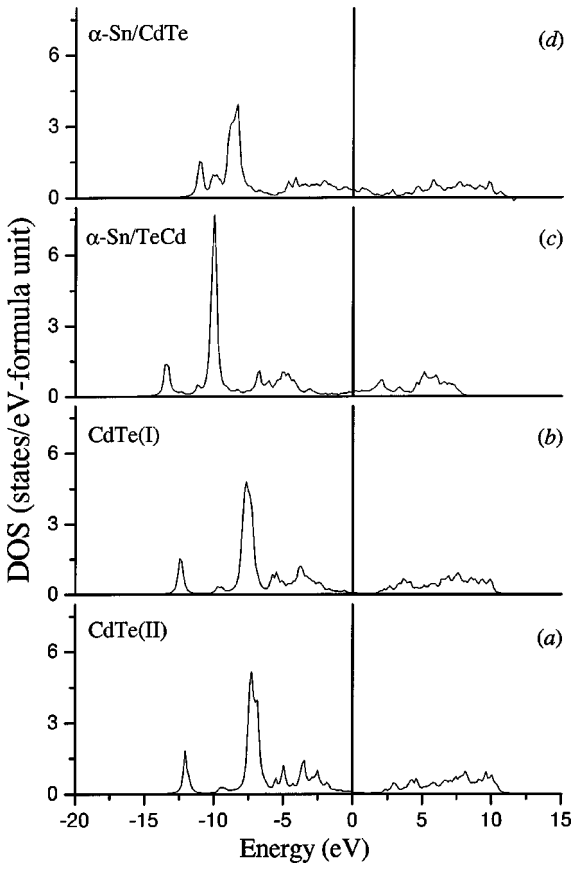

FIG. 9. Cd and Te partial densities of states in different environments: (a) bulk CdTe(II) with the cluster centered on Te, (b) bulk CdTe(I) with the cluster centered on Cd, (c) α-Sn/TeCd interface layers, and (d) α-Sn/CdTe interface layers.

of Cd $4d$ spectra toward higher energy was indeed observed by Tang *et al.*[14] for (001) interfaces; however, the absolute value of shift measured was only 0.24 eV. The energy difference is mostly due to excited state core-hole relaxation effects not included in the present (ground state) calculations. In Fig. 9(c) we note a strong perturbation of the Te plus Cd VB states for atoms neighboring the Sn/TeCd interface, consisting of valence band broadening and a shift of the Cd $4d$ peak to lower energy. The Sn/CdTe interface, while structurally more extreme than that of Sn/TeCd, shows a similar but weaker VB displacement with the Cd $4d$ peak shifted ~ 3 eV to greater binding energy. These VB shifts correspond to potential shifts due to charge transfer and bonding interactions at the interface, and are the local representation counterpart of much-discussed ''band-bending'' effects found in band-structure approaches to interfaces.

Mulliken population analysis of the valence orbital distributions and net atomic charges for each of the systems studies is presented in Table IV. Net atomic charges are defined as the atomic number Z minus the total electron population on the atom. For both bulk Sn phases we see an sp hybridization characteristic of the Sn-Sn bonding interactions, while the α-Sn surface layer Sn_S shows a charge transfer of $\sim 0.15e$, mostly to the neighboring Sn_{S-1} layer. The corresponding tin layers in contact with the Sn/CdTe or Sn/TeCd interfaces typically show a lesser charge transfer, $Q \leqslant 0.1e$, except for the highly perturbed interpenetrating case of α-Sn/CdTe ($d = -0.79$ Å) and short-distance case of α-Sn/TeCd ($d = 1.06$ Å), both unstable configurations. Thus we may conclude that in the vicinity of the CdTe substrate, Sn remains essentially neutral; $5s$-$5p$ hybridization is also present in the α-Sn layers on CdTe.

The isomer shift and quadrupole splitting at the central atom Sn_I site were calculated for bulk α-Sn, β-Sn, for an α-Sn(001) surface, and α-Sn/CdTe(001) and α-Sn/TeCd(001) interfaces for different bi-crystal distances. Theoretical results for the two phases of bulk tin, along with experimental data, were given in Table II; analysis of the interfaces is shown in Tables V and VI. The calculated IS difference between α-Sn and β-Sn of -0.41 mm/sec is in reasonably good agreement with the experimental value of -0.52 mm/sec, using the previously derived calibration factor of $0.0844 a_0^3$ mm/s.[37] Use of the more recent calibration by Svane *et al.*[7] would make the agreement essentially perfect. Thus we may have some confidence in the variation of the IS with the surface-vacuum interface and variation with the Sn/CdTe interface distance displayed in Table V.

The mechanisms responsible for variations in the IS are charge transfer and volume (or orthogonality) effects. To explain the values of the IS displayed in Table V, we first note

TABLE V. Nonrelativistic valence charge density $\rho(0)$, isomer shift (IS), and $5s$ Mulliken population for bulk β-Sn (central atom), bulk α-Sn (central atom), and α-Sn surface (central atom at surface layer), and at the Sn_I sites for α-Sn/CdTe and α-Sn/TeCd interfaces.

System	Interface layers d (Å)	$\rho(0)$ (a_0^{-3})	IS[a] (mm/s)	$5s$ population
β-Sn (bulk)	-	24.51	0.00	1.73
α-Sn (bulk)	-	22.39	−0.41	1.64
α-Sn (surface)	-	27.95	0.67	1.85
α-Sn/CdTe	1.62	23.86	−0.13	1.77
	0.53	23.04	−0.29	1.67
	0.00[b]	23.48	−0.20	1.68
	−0.79	25.33	0.16	1.74
α-Sn/TeCd	1.85[b]	27.68	0.62	1.78
	1.62	27.44	0.57	1.75
	1.53	27.32	0.55	1.74
	1.06	26.29	0.35	1.67

[a] $\alpha = 0.0844 a_0^3$ mm/s, from Ref. 37. The correction factor $S'(Z)$ for relativistic effects is 2.306 (from Ref. 38). Values of the IS are given relative to β-Sn.
[b] Minimum-energy configuration.

TABLE VI. Electric field gradient V_{ZZ}, asymmetry parameter η, and quadrupole splitting (QS), for β-Sn, bulk α-Sn, and α-Sn surface, and at the Sn_I sites for α-Sn/CdTe and α-Sn/TeCd. The interface layer distance d is given in Å.

System	Interface d	V_{ZZ} $(10^{17}$ V/cm$^2)$	V_{ZZ} (a_0^{-3})	η	QS[a] (mm/s)
β-Sn	-	10.91	1.12	0.0	−0.75
α-Sn	-	0	0	–	0
α-Sn (surface)	-	40.46	4.16	0.42	−2.85
α-Sn/CdTe	1.62	−7.73	−0.80	0.55	0.55
	0.53	−38.48	−3.96	0.11	2.64
	0.00[b]	−36.07	−3.71	0.24	2.49
	−0.79	−15.42	−1.59	0.77	1.15
α-Sn/TeCd	1.85[b]	33.00	3.40	0.33	−2.30
	1.62	34.90	3.59	0.22	−2.41
	1.53	35.33	3.64	0.15	−2.43
	1.06	32.95	3.39	0.12	−2.26

[a] $Q = -0.109$ barn, from Ref. 39.
[b] Minimum-energy configuration.

that no correlation is found between the IS and the charges Q on Sn (see Table IV). On the other hand, a clear relation exists between the IS and the Sn $5s$ population, for α-Sn, β-Sn, the α-Sn(001) surface, and the α-Sn/CdTe interface at several distances (see Table V). Since in the non-relativistic approach this orbital is solely responsible for the valence density at the Sn nucleus, it is thus seen that the IS should be directly proportional to its population. In particular, the large value of the IS at the α-Sn surface is seen to be due to a loss of $5s$-$5p$ hybridization brought about by the decrease in coordination of the surface atoms, and the consequent shift toward the free atom $5s^2 5p^2$ configuration.

In the case of the interface α-Sn/TeCd, a clear proportionality between the IS and the $5s$ population exists among the several distances. However, it may be observed that for this Sn-Te interface all the ISs are shifted to higher values. This may be tentatively ascribed to a ''volume contraction'' effect of the Sn valence wavefunctions, caused by the extended valence functions of the neighboring Te negative ions at the interface. As for the core functions of Sn, which were kept ''frozen'' in the calculations, it was considered that their contribution to $\rho(0)$ is approximately the same in the different cases, and thus do not contribute to the IS.

The predicted structural variations of the QS are more dramatic, ranging from the symmetry-imposed value of zero in α-Sn to -0.75 mm/sec in β-Sn, to -2.85 mm/sec on a free (001) α-Sn surface, as may be seen in Table VI. We note here that the calculated QSs represent *semicore and valence* contributions $(4d,5p)$ to the electric field gradient only; the omitted deep-core polarization terms could be expected to reduce the predicted values slightly. Large QSs are expected in the reduced symmetry of surfaces and interfaces; for example, electrodeposited monolayer and submonolayer Sn films on Pt were observed with $|\mathrm{QS}| \geqslant 1.4$ mm/sec.[40] The calculated strong variation of magnitude of the QS and its characteristic sign (oblate/prolate distortion of ρ) with interface chemical nature and interlayer distance suggests the utility of future measurements on very thin films.

The direction of V_{zz} is in the plane of the (001) surface of α-Sn, and in the Sn_I plane of the interface in α-Sn/CdTe and α-Sn/TeCd, for all distances. The contribution of the surrounding screened nuclei [see Eq. (3)] is much smaller than the electronic contribution to V_{zz}, typically about 10%. The electric-field gradients at Sn_I of the interface have opposite signs in Sn/CdTe and Sn/TeCd. The valence V_{zz} around a Sn nucleus is produced by the anisotropic filling of the $5p_x$, $5p_y$, and $5p_z$ orbitals, as well as spatial distortions of the valence functions which may be different in different directions. The complex combination of these factors results in the calculated values in Table VI.

Contour maps of electronic charge density are given in Figs. 10 and 11 for the energy-minimum geometries of Sn/TeCd and Sn/CdTe, respectively, in a plane perpendicular to the interface. In Fig. 10 we clearly see the formation of ionic-covalent bonds between Sn and Te in the central Sn_ITe_I layers, and can compare the interlayer packing due to the somewhat large Te compared to Sn to that seen in the pure-tin region. The apparently empty regions are simply due to the offset of alternating atom planes (*ABCDABCD...*) above and below the plotting plane. The Cd_ISn_I alloy layer of Sn/CdTe is dramatically evident in Fig. 11. It is interesting that if one considers *metallic radii* only, such a packing would appear unfavorable; however, the positive charge on Cd results in a considerably reduced ionic radius, compatible with the predicted structure.

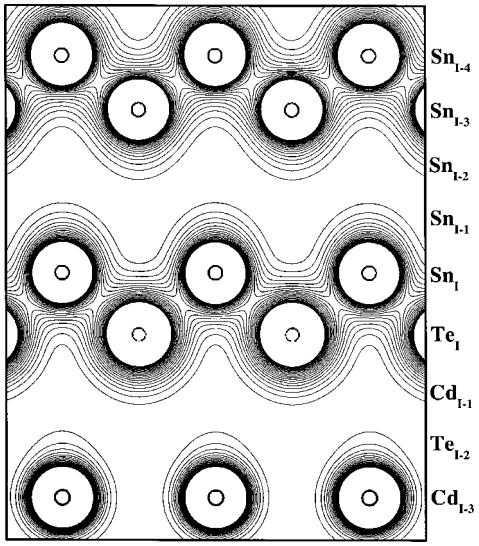

FIG. 10. Contour map of the electronic charge density $\rho(\mathbf{r})$ in a plane perpendicular to the interface layers of α-Sn/TeCd cluster, at the equilibrium structural configuration. Contours vary from $0.0e/a_0^3$ to $0.1e/a_0^3$ with intervals $5.0\times10^{-3}e/a_0^3$.

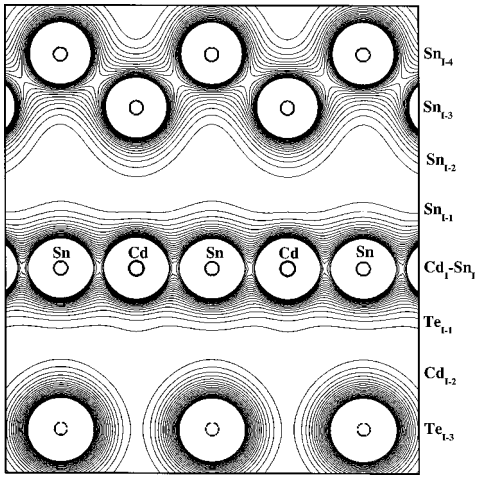

FIG. 11. Contour map of the electronic charge density $\rho(\mathbf{r})$ in a plane perpendicular to the interface layers of α-Sn/CdTe at the equilibrium structural configuration. Contour specifications as in Fig. 10.

V. CONCLUSIONS

Films of α-Sn(001) of thickness ~2000 Å enriched in ^{119}Sn were grown by molecular beam epitaxy on CdTe (001) wafers, and were found to be stable up to a temperature of ~130 °C. Nuclear resonant scattering at 23.88 keV was measured, using a novel spectrometer with a resolution of ~1 meV, revealing a local phonon density of states indistinguishable from that of bulk α-Sn. Conventional Mössbauer spectroscopy was used in the scattering mode, verifying hyperfine parameters to be those of bulk α-Sn, and observing the high temperature transformation to β-Sn. Density functional embedded cluster calculations were carried out for both bulk phases of tin, for an α-Sn(001) free surface, and for bicrystals with structures of α-Sn(001)/CdTe and α-Sn(001)/TeCd. Although, due to sample thickness, both experiments revealed properties essentially of the bulk, the calculations presented here allow an investigation of surface and interface regions at an atomic level, thus providing complementary information. Therefore, calculations were performed for bulk α-Sn and β-Sn, for calibration and comparison with experiments, as well as for free surfaces and interfaces, for which no data were obtained and thus predictions were made. Effects of interlayer relaxation were explored, by allowing rigid translation of α-Sn along the [001] axis; for the Sn/CdTe case the minimum energy configuration was found for a mixed Sn/Cd interface layer similar to that suggested on the basis of photoemission studies of (111) interfaces. For Sn/TeCd the minimum energy is found for a surface layer spacing Sn_I-Te_I of $d=1.85$ Å, somewhat expanded compared to bulk α-Sn, and consistent with the larger Te anion radius. The Mössbauer isomer shift and quadrupolar splitting were found to be surface and interface sensitive, IS values of ~0.6 mm/s (relative to β-Sn) being predicted for free surface and for the Sn_I layer of Sn/TeCd. Reduced symmetry at the interfaces, and lowered atomic coordination induces QS values of magnitude 2.3–2.9 mm/s in the various cases, which would be easily detectable in interface-sensitive measurements, e.g., on multilayer heterojunctions. The observed shift of near-interface Cd $4d$ semicore levels to greater binding energies was also seen in calculated densities of states. Charge density maps of the Sn/CdTe and Sn/TeCd interface regions permit visualization of the contrast between Sn-Cd metallic bonding and Sn-Te ionic-covalent charge transfer predicted for the two structures, and made quantitative by Mössbauer IS and QS values.

In view of difficulties encountered in attempts to grow multilayer Sn/CdTe and related structures, and experimental evidence of surface roughening, formation of microcrystalline SnTe, etc., we suggest that an atomistic modeling of these interfaces could be useful in better understanding chemical reactions there and in developing improved growth strategies. The large number of degrees of chemical and structural freedom preclude the direct application of first-principles methods; however, such methods would be important in validating structures proposed on the basis of simulations. The INRS technique permits a rapid measurement of *local* vibrational structures associated with the tin site, information obtained previously only with great difficulty. Applications to additional Sn-containing compounds, alloys, and biologically active systems will be presented elsewhere.

ACKNOWLEDGMENTS

This work was supported by CNPq and by the U.S. National Science Foundation, under the MRSEC program at Northwestern University, Grant No. DMR-0076097. Calculations were carried out in part at the Supercomputing Center of the Federal University of Rio Grande de Sul, Brazil.

[1] L-W Tu, G. K. Wong, and J. B. Ketterson, Appl. Phys. Lett. **55**, 1327 (1989).
[2] S. Takatani and Y. W. Chung, Phys. Rev. B **31**, 2290 (1985).
[3] A. Continenza and A. J. Freeman, Phys. Rev. B **45**, 5953 (1992).
[4] A. Continenza and A. J. Freeman, Phys. Rev. B **43**, 8951 (1991).
[5] S. Groves and W. Paul, Phys. Rev. Lett. **11**, 194 (1963); W. Zawadzki and J. Kowalski, Solid State Commun. **15**, 303 (1974); T. Brudevoll, D. S. Citrin, M. Cardona, and N. E. Christensen, Phys. Rev. B **48**, 8629 (1993).
[6] B. Akdim, D. A. Papaconstantopoulos, and M. J. Mehl, Phys. Rev. B **82**, 47 (2002).
[7] A. Svane, N. E. Christensen, C. O. Rodriguez, and M. Methfessel, Phys. Rev. B **55**, 12 572 (1997).
[8] B. I. Craig and B. J. Garison, Phys. Rev. B **33**, 8130 (1986).
[9] L. W. Tu, G. K. Wong, and J. B. Ketterson, Appl. Phys. Lett. **54**, 1010 (1989).
[10] H. Zimmerman, R. C. Keller, P. Meisen, and M. Seelmann-Eggebert, Surf. Sci. **377–379**, 904 (1997).
[11] A. Dittmar-Wituski and P. J. Møller, Surf. Sci. **287**, 577 (1993).
[12] H. Höchst, D. W. Niles, and I. Hernández-Calderón, J. Vac. Sci. Technol. B **6**, 1219 (1988).
[13] I. Hernández-Calderón and H. Höchst, J. Phys.: Condens. Matter **5**, A327 (1993).
[14] M. Tang, D. W. Niles, I. Hernández-Calderón, and H. Höchst, Phys. Rev. B **36**, 3336 (1987).
[15] B. F. Mason and B. R. Williams, Surf. Sci. **277**, 77 (1992).
[16] A. B. Villaflor, K. Shimomura, K. Kawamura, A. I. Belogorokhov, and M. Kimata, J. Cryst. Growth **150**, 779 (1995).
[17] B. Freytag, U. Rössler, K. Karch, G. H. Grosch, and K.-J. Range, J. Chem. Phys. **99**, 6751 (1993); G. H. Grosch, B. Freytag, K.-J. Range, and U. Rössler, Int. J. Quantum Chem. **52**, 919 (1994).
[18] M. Seto, Y. Yoda, S. Kikuta, X. W. Zhang, and M. Ando, Phys. Rev. Lett. **74**, 3828 (1995).
[19] W. Sturhahn, T. S. Toellner, E. E. Alp, X. Zhang, M. Ando, Y. Yoda, S. Kikuta, M. Seto, C. W. Kimball, and B. Dabrowski, Phys. Rev. Lett. **74**, 3832 (1995).
[20] W. Sturhahn and V. G. Kohn, Hyperfine Interact. **123/124**, 367 (1999).
[21] A. I. Chumakov and W. Sturhahn, Hyperfine Interact. **123/124**, 781 (1999).
[22] M. Y. Hu, PhD thesis, Northwestern University, 1998.
[23] M. Y. Hu, T. S. Toellner, W. Sturhahn, P. M. Hession, J. P. Sutter, and E. E. Alp, Nucl. Instrum. Methods Phys. Res. A **430**, 271 (1999).
[24] M. Y. Hu, W. Sturhahn, T. S. Toellner, P. M. Hession, J. P. Sutter, and E. E. Alp, Nucl. Instrum. Methods Phys. Res. **428**, 551 (1999).
[25] W. Sturhahn and A. Chumakov, Hyperfine Interact. **123/124**, 809 (1999).
[26] P. Pavone, S. Baroni, and S. de Gironcoli, Phys. Rev. B **57**, 10 421 (1998).
[27] D. L. Price, J. M. Rowe, and R. M. Nicklow, Phys. Rev. B **3**, 1268 (1971).
[28] B. Roldan-Cuenya, W. Keune, W. Sturhahn, T. S. Tollner, and M. Y. Hu, Phys. Rev. B **64**, 235321 (2001).
[29] J. G. Stevens, Hyperfine Interact. **13**, 221 (1983).
[30] J. K. Lees and P. A. Flinn, J. Chem. Phys. **48**, 882 (1968).
[31] R. G. Parr and W. Yang, *Density Functional Theory of Atoms and Molecules* (Oxford University Press, New York, 1989); J. Callaway and N. H. March, in *Solid State Physics*, edited by H. Ehrenreich and D. Turnbull (Academic, New York, 1984); *Density Functional Theory of Molecules, Clusters, and Solids* edited by D. E. Ellis (Kluwer Academic, Dordrecht, 1995).
[32] E. J. Baerends, D. E. Ellis, and P. Ros, Chem. Phys. **2**, 41 (1973); B. Delley and D. E. Ellis, J. Chem. Phys. **76**, 1949 (1982); D. E. Ellis and J. Guo, in *Density Functional Theory of Molecules, Clusters, and Solids* (Ref. 31), p. 263; D. E. Ellis and D. Guenzburger, Adv. Quantum Chem. **34**, 51 (1999); D. E. Ellis and O. Warschkow, *ibid.* (to be published).
[33] S. H. Vosko, L. Wilk, and M. Nusair, Can. J. Phys. **58**, 1200 (1980).
[34] A. D. Becke, Phys. Rev. A **38**, 3098 (1988).
[35] J. P. Perdew, Phys. Rev. B **33**, 8822 (1986); **34**, 7406 (1986).
[36] D. E. Parry, Surf. Sci. **49**, 433 (1975); **54**, 195 (1976).
[37] J. Terra and D. Guenzburger, J. Phys.: Condens. Matter **3**, 6763 (1991).
[38] D. A. Shirley, Rev. Mod. Phys. **36**, 339 (1964).
[39] H. Haas, M. Menningen, H. Andreasen, S. Damgaard, H. Grann, F. T. Pedersen, J. W. Petersen, and G. Weyer, Hyperfine Interact. **15/16**, 215 (1983).
[40] B. J. Bowles and T. E. Cranshaw, Phys. Lett. **17**, 258 (1965).